From a single-band metal to a high-temperature superconductor via two thermal phase transitions

Rui-Hua He,[1,2,3*] M. Hashimoto,[1,2,3*] H. Karapetyan,[1,2] J. D. Koralek,[3,4]
J. P. Hinton,[3,4] J. P. Testaud,[1,2,3] V. Nathan,[1,2] Y. Yoshida,[5] Hong Yao,[1,3,4]
K. Tanaka,[1,2,3,6] W. Meevasana,[1,2,7] R. G. Moore,[1,2] D. H. Lu,[1,2] S.-K. Mo,[3]
M. Ishikado,[8] H. Eisaki,[5] Z. Hussain,[3] T. P. Devereaux,[1,2†]
S. A. Kivelson,[1†] J. Orenstein,[3,4†] A. Kapitulnik,[1,2†] Z.-X. Shen[1,2†]

[1]Geballe Laboratory for Advanced Materials, Departments of Physics
and Applied Physics, Stanford University, Stanford, California 94305, USA
[2]Stanford Institute for Materials and Energy Sciences,
SLAC National Accelerator Laboratory, Menlo Park, California 94025, USA
[3]Advanced Light Source and Materials Sciences Division,
Lawrence Berkeley National Laboratory, Berkeley, California 94720, USA
[4]Department of Physics, University of California, Berkeley, CA 94720
[5]Nanoelectronics Research Institute, AIST, Ibaraki 305-8568, Japan
[6]Department of Physics, Osaka University, Toyonaka, Osaka 560-0043, Japan
[7]School of Physics, Suranaree University of Technology, Nakhon Ratchasima, 30000 Thailand
[8]Japan Atomic Energy Agency, Tokai, Ibaraki 319-1195, Japan
[*]These authors contributed equally to this work.
[†]To whom correspondence should be addressed; E-mail: zxshen@stanford.edu,
aharonk@stanford.edu, jworenstein@lbl.gov, kivelson@stanford.edu, tpd@stanford.edu.

The nature of the pseudogap phase of cuprate high-temperature superconductors is one of the most important unsolved problems in condensed matter physics. We studied the commencement of the pseudogap state at temperature T^* using three different techniques (angle-resolved photoemission spectroscopy, polar Kerr effect, and time-resolved reflectivity) on the same optimally-doped Bi2201 crystals.

1

We observe the coincident onset at T^* of a particle-hole asymmetric antinodal gap, a non-zero Kerr rotation, and a change in the relaxational dynamics, consistent with a phase transition. Upon further cooling, spectroscopic signatures of superconductivity begin to grow close to the superconducting transition temperature (T_c), entangled in an energy-momentum dependent fashion with the pre-existing pseudogap features.

As complex oxides, cuprate superconductors belong to a class of materials which exhibit many broken-symmetry states; unravelling the relationship between superconductivity in the cuprates and other possible broken-symmetry states has been a major challenge of condensed matter physics. A possibly related issue concerns the nature of the pseudogap in the cuprates and its relationship with superconductivity. Angle-resolved photoemission spectroscopy (ARPES) studies have shown that the pseudogap develops below a temperature T^* near the Brillouin zone boundary while preserving a gapless Fermi arc near the zone diagonal (*1*). A key issue is the extent to which the pseudogap is a consequence of superconducting fluctuations (*2–5*), which should exhibit a rough particle-hole symmetry, or another form of (incipient) order (*6–12*), which typically should induce particle-hole asymmetric spectral changes. Candidate orders include various forms of density wave, nematic or unconventional magnetic orders that break different combinations of lattice translational (*6–8, 13– 19*), rotational (*6, 9, 15, 17, 20–22*), and time-reversal (*7, 9, 23–26*) symmetries.

We have focused on crystals of nearly optimally-doped (OP) $Pb_{0.55}Bi_{1.5}Sr_{1.6}La_{0.4}CuO_{6+\delta}$ (Pb-Bi2201, $T_c = 38$ K, $T^* = 132 \pm 8$ K) (*27*), and combined the ARPES measurements of the evolution of the band structure over a wide range of temperature, momentum and energy, with high-precision measurements of the polar Kerr effect (PKE) and time-resolved reflectivity (TRR). Bi2201 was chosen to avoid the complications resulting from bilayer splitting and strong antinodal bosonic mode coupling inherent to $Bi_2Sr_2CaCu_2O_{8+\delta}$ (Bi2212) (*1*). Whereas ARPES is a surface probe, PKE enables us to monitor a bulk, thermodynamic (via the fluctuation-dissipation theorem)

property which has proven (*28*) to be a sensitive probe of the onset of a broken-symmetry state, and TRR gives complementary information on the bulk, near-equilibrium dynamics of the system.

We will first analyze our ARPES data collected in different temperature regions. Above T^*, Pb-Bi2201 has a simple one-band band structure (right side of Fig. 1). For each cut in momentum space perpendicular to Γ-M $[(0,0)$-$(\pi,0)]$ (C1-C7 in Fig. 1), the only distinct feature in the corresponding Fermi-function-divided (*27*) energy distribution curves (EDCs) is a maximum (red circles in Fig. 2, A-G). As a function of the y component of the wave vector (k_y), the maxima have an approximately parabolic dispersion for each cut (red circles in Fig. 2, O-U); the band bottom lies on the Γ-M axis, and the dispersion crosses the Fermi level (E_F) at two momenta, k_F (k_{F1} and k_{F2}). The band-bottom binding energy monotonically decreases from near Γ to M (Fig. 2, O-U). We take the Fermi-level crossings of this single band to define the Fermi surface. Despite the simplicity of the electronic structure above T^*, the width and energy-dependent broadening of the EDC maximum features, along with the familiar strange metal behavior seen in transport, imply that the system is not well described as a Fermi liquid.

We now turn to the temperature region below T_c. Here, the entire Fermi surface is gapped except at the nodal points (k_F lying on the zone diagonal). In the nodal region, consistent with previous reports (*4, 5, 11, 12*), a d-wave-like gap along the Fermi surface is observed which we quantify as the energy position of the EDC maximum (blue circles) at k_F (Fig. 2, L-N). This maximum is still the only identifiable feature in the EDC. By comparing the EDCs in Fig. 2, E-G with those in Fig. 2, L-N, we see that the peaks of EDCs near k_F are much sharper below T_c than above T^*, however (perhaps surprisingly) the peaks well away from k_F appear broader but with larger experimental uncertainties (also see Fig. 2, V-W).

Away from the nodal region, the dispersion along each cut rises to a minimum binding energy and then bends back (Fig. 2, H-K). These back-bendings (black arrows in Fig. 2, O-S) occur at momenta k_G (k_{G1} and k_{G2}), which are increasingly separated from the Fermi surface (compare blue

and red squares on the left side of Fig. 1) towards the antinodes (k_F lying on the zone boundary). Note that, for a superconducting gap, as a consequence of the particle-hole symmetry, one would expect $k_G \cong k_F$ (Fig. S6), as is the case in the nodal region. The substantial $k_G - k_F$ misalignment, previously found in a single antinodal cut perpendicular to Γ-M, has been interpreted as a signature of non-particle-hole symmetric order (*29*). Our observation here complements that finding by providing an entire momentum-space picture.

The width and shape of the EDC near k_F change fairly abruptly as a function of position along the Fermi surface, in contrast with the smooth evolution seen above T^* (compare magenta curves in Fig. 2, H-N and A-G). Strikingly, the antinodal EDC maxima below T_c are broader than those above T^* (Figs. 2, V-W and S7I). Such broadening of the antinodal spectra with decreasing temperature, as reported previously (*29*), is likely intrinsic, as the expected sharpening is observed simultaneously in the nodal spectra at low energy.

Around the M point, both the EDC line shape and the dispersion of the EDC maxima are more complex than their counterparts above T^*. The dispersion of the EDC maxima has two separate branches, one at relatively low energy which shows back-bendings at k_G and the other at higher energy around the band bottom on the Γ-M axis. As one moves from cuts C1 to C7, the apparent discontinuity between the two branches near the antinode vanishes and the two branches merge (Fig. 2, O-U). Both k_G (blue squares in Fig. 1) and the band-bottom energy (blue circles in Fig. 2W) evolve smoothly, even as the dispersion at intermediate energies changes dramatically.

Along with the changes in the dispersion of the EDC maxima below T_c, a well-defined shoulder feature (green dots in Fig. 2, H-K and W) (*27*) emerges at low energy in the EDCs. This feature exhibits little dispersion either along Γ-M (Fig. 2W) or perpendicular to it (Fig. 2, H-J). Unlike the EDC maxima, its dispersion does not continue towards the zone center (Fig. 2W) but instead loses its definition away from the vicinity of the M point (magenta-shaded region in Fig. 1).

The changes in the spectral function on cooling do not occur smoothly; instead, abrupt changes

in the thermal evolution occur in the neighborhoods of T^* and T_c.

A detailed temperature-dependent study of an antinodal cut (C1 in Fig. 1) shows that the dispersion of the EDC maxima (blue circles in Fig. S1, A-E) exhibit a transformation which begins at a temperature equal (within experimental uncertainty) to the reported values of T^* in the literature (*27*). Specifically, the energies of the EDC maxima at the band bottom and at k_F are temperature independent above T^* but begin shifting to higher binding energies below T^* (Fig. S1F). The energy position at k_F is the measure of the pseudogap, and can be defined as a spectral order parameter that becomes non-zero below T^*. Moreover, at temperatures below T^* but well above T_c, one can already see the $k_G - k_F$ misalignment developing (right inset of Fig. 3). These observations are consistent with our previous report on a similar cut in an OP Pb-Bi2201 sample prepared under a different post-annealing condition (*29*).

It would be natural (as discussed below) to associate the abrupt change in nature of the ARPES spectra with a transition to a broken-symmetry state below T^*. To test this idea, we performed PKE measurements on the same crystals with finely-spaced temperature steps (*27*). The results (Fig. 3) are clearly suggestive of a slightly-rounded phase transition at T^* below which a finite Kerr rotation emerges. A similar transition in the Kerr rotation was previously observed in high-quality $YBa_2Cu_3O_{6+x}$ (YBCO) crystals and was suggested to be linked to a broken-symmetry state that is not necessarily magnetic in nature (*25*). The smallness of the previously observed Kerr rotation in YBCO suggested that it might not reflect the primary order. The present data again show a small Kerr rotation; however, the strong correspondence between the ARPES and PKE data in Fig. 3, allows us to conjecture a phase transition at T^*, and also to corroborate the interpretation of previously published data on YBCO in terms of a similar transition.

We also performed TRR measurements on the same Pb-Bi2201 crystals (*27*). Upon laser pumping at temperatures between T_c and T^*, we observed a negative transient reflectivity change with a fast time-resolution-limited turn-on followed by a decay on the order of 100 femtoseconds (Fig.

S3). Additionally, we observed a TRR signal of the opposite sign which emerges below T_c and is characterized by a slow rise time followed by a decay on the order of picoseconds. Both signals have previously been seen in YBCO (*30, 31*), $Tl_2Ba_2Ca_2Cu_3O_y$ (*32*) and Bi2212 (*33*), with the one dominating below T_c ascribed to photo-induced pair breaking and the one above T_c associated with the pseudogap state. The uniqueness of the current study lies in its direct correspondence with ARPES and PKE. As shown in the left inset of Fig. 3, the magnitude of the negative TRR signal overall tracks the ARPES and PKE data quite well and shows a sharp onset at T^*. This added correspondence further supports the existence of a phase transition at T^* into the pseudogap state with near-equilibrium dynamics distinct from superconductivity.

Upon cooling below T_c, it is observed in ARPES that the shoulder on the low-energy side of the EDC maximum appears to develop somewhat above T_c but well below T^*, and it grows truly distinct only below T_c (compare Figs. 4, A-B and S1, A-E). In order to obtain a clearer view of the structure of this feature, we show, in the insets of Fig. 4, E-G, the spectra at low temperatures divided by the one at 60K - a procedure that converts the shoulder into a small peak. In Fig. 4C we adopt the same procedure, but dividing by the 40K spectra instead, and in Fig. S2 we have subtracted off an approximate background from the EDCs. All three methods of analysis produce qualitatively similar results, with a small peak at a position that does not disperse appreciably along the exemplary antinodal Cut C1. In all cases, the energy and width of the peak do not change significantly with increasing temperature, while the peak intensity is strongly temperature-dependent; the peak becomes undetectable at a temperature which, while greater than T_c, is nowhere near T^*. This behavior of the processed data is highly reminiscent of the behavior of the superconducting coherence peak in Bi2212 (*34*), although that peak is visible in the raw data (Fig. 4D).

The strong and analogous temperature dependences of the ARPES, PKE and TRR data seen between T_c and T^* are most naturally understood if T^* is associated with a phase transition to a non-superconducting broken-symmetry state (*27*). While superconducting fluctuations are observable

above T_c (Figs. 4, E-G and S2E), they appear to peter out at too low temperatures ($\lesssim 60$ K) to play a central role in this higher temperature transition. To complete this picture, it is necessary to identify the nature of the broken-symmetry state, and to relate it to the apparently similar electronic changes that occur below T^* in other cuprates (27).

Below T_c, the nodal arc is gapped with a d-wave-like structure suggestive of a dominantly superconducting origin (35). In contrast, in the antinodal region, rather than one order being dominant, or the two gaps of both orders adding in quadrature, the spectral function develops a complex structure with two energy scales of mixed origin, a larger one being primarily associated with the pseudogap order, and a smaller one with the superconducting order.

To see what can be learned about the pseudogap order from ARPES, we have used a simple mean-field model (27) to compute the expected changes to the band structure induced by various forms of density wave (6–8, 13–19) (Fig. S7) or nematic order (6, 15, 17, 20–22) (Fig. S8) coexisting with d-wave superconductivity. We note that some (but certainly not all) key aspects of our experimental observations can be qualitatively reproduced, regardless of which of these orders is assumed (27). An essential feature of both the experiment and the fits is the comparable sizes of the superconducting gap and the pseudogap. This suggests that the two orders may have a more intimate connection than just competing orders, such as seen in $2H$-NbSe$_2$ where the charge density wave gap is at least 3 times the superconducting gap (37).

References and Notes

1. A. Damascelli, Z. Hussain, Z.-X. Shen, Angle-resolved photoemission studies of the cuprate superconductors. *Rev. Mod. Phys.* **75**, 473 (2003).

2. V. J. Emery, S. A. Kivelson, Importance of phase fluctuations in superconductors with small superfluid density. *Nature* **374,** 434 (1995).

3. Y. Wang, L. Li, N. P. Ong, Nernst effect in high-T_c superconductors. *Phys. Rev. B* **73,** 024510 (2006).

4. K. Nakayama *et al.*, Evolution of a pairing-induced pseudogap from the superconducting gap of $(Bi, Pb)_2Sr_2CuO_6$. *Phys. Rev. Lett.* **102,** 227006 (2009).

5. J. Meng *et al.*, Monotonic d-wave superconducting gap of the optimally doped $Bi_2Sr_{1.6}La_{0.4}CuO_6$ superconductor by laser-based angle-resolved photoemission spectroscopy. *Phys. Rev. B* **79,** 024514 (2009).

6. S. A. Kivelson, E. Fradkin, V. J. Emery, Electronic liquid-crystal phases of a doped Mott insulator. *Nature* **393,** 550 (1998).

7. S. Chakravarty, R. B. Laughlin, D. K. Morr, C. Nayak, Hidden order in the cuprates. *Phys. Rev. B* **63,** 094503 (2001).

8. M. Grilli, G. Seibold, A. Di Ciolo, J. Lorenzana, Fermi surface dichotomy in systems with fluctuating order. *Phys. Rev. B* **79,** 125111 (2009).

9. C. M. Varma, Non-Fermi-liquid states and pairing instability of a general model of copper oxide metals. *Phys. Rev. B* **55,** 14554 (1997).

10. K. Tanaka *et al.*, Distinct Fermi-momentum-dependent energy gaps in deeply underdoped Bi2212. *Science* **314,** 1910 (2006).

11. T. Kondo *et al.*, Disentangling Cooper-pair formation above T_c from the pseudogap state in the cuprates. *Nat. Phys.* **7,** 21 (2011).

12. J.-H. Ma *et al.*, Coexistence of competing orders with two energy gaps in real and momentum space in the high temperature superconductor $Bi_2Sr_{2-x}La_xCuO_{6+\delta}$. *Phys. Rev. Lett.* **101,** 207002 (2008).

13. J. M. Tranquada, B. J. Sternlieb, J. D. Axe, Y. Nakamura, S. Uchida, Evidence for stripe correlations of spins and holes in copper oxide superconductors. *Nature* **375,** 561 (1995).

14. J. E. Hoffman *et al.*, A four unit cell periodic pattern of quasi-particle states surrounding vortex cores in $Bi_2Sr_2CaCu_2O_{8+\delta}$. *Science* **295,** 466 (2002).

15. C. Howald, H. Eisaki, N. Kaneko, A. Kapitulnik, Coexistence of periodic modulation of quasi-particlestates and superconductivity in $Bi_2Sr_2CaCu_2O_{8+\delta}$. *Proc. Natl. Acad. Sci.* **100,** 9705 (2003).

16. M. Vershinin *et al.*, Local ordering in the pseudogap state of the high-T_c superconductor $Bi_2Sr_2CaCu_2O_{8+\delta}$. *Science* **303,** 1995 (2004).

17. Y. Kohsaka *et al.*, An intrinsic bond-centered electronic glass with unidirectional domains in underdoped cuprates. *Science* **315,** 1380 (2007).

18. C. V. Parker *et al.*, Fluctuating stripes at the onset of the pseudogap in the high-Tc supercon-ductor $Bi_2Sr_2CaCu_2O_{8+x}$. *Nature* **468,** 677 (2010).

19. W. D. Wise *et al.*, Charge density wave origin of cuprate checkerboard visualized by scanning tunneling microscopy. *Nature Phys.* **4,** 696 (2008).

20. V. Hinkov *et al.*, Electronic liquid crystal state in the high-temperature superconductor $YBa_2Cu_3O_{6.45}$. *Science* **319,** 597 (2008).

21. R. Daou *et al.*, Broken rotational symmetry in the pseudogap phase of a high-T_c superconductor. *Nature* **463,** 519 (2010).

22. M. J. Lawler *et al.*, Intra-unit-cell electronic nematicity of the high-T_c copper-oxide pseudogap states. *Nature* **466,** 347 (2010).

23. A. Kaminski *et al.*, Spontaneous breaking of time-reversal symmetry in the pseudogap state of a high-T_c superconductor. *Nature* **416,** 610 (2002).

24. B. Fauqu$é$ *et al.*, Magnetic order in the pseudogap phase of high-T_c superconductors. *Phys. Rev. Lett.* **96,** 197001 (2006).

25. J. Xia *et al.*, Polar Kerr-effect measurements of the high-temperature $YBa_2Cu_3O_{6+x}$ superconductor: Evidence for broken symmetry near the pseudogap temperature. *Phys. Rev. Lett.* **100,** 127002 (2008).

26. Y. Li *et al.*, Unusual magnetic order in the pseudogap region of $HgBa_2CuO_{4+\delta}$. *Nature* **455,** 372 (2008).

27. See supporting material on *Science* Online.

28. J. Xia, Y. Maeno, P. T. Beyersdorf, M. M. Fejer, A. Kapitulnik, High resolution polar Kerr effect measurements of Sr_2RuO_4: Evidence for broken time-reversal symmetry in the superconducting state. *Phys. Rev. Lett.* **97,** 167002 (2006)

29. M. Hashimoto *et al.*, Particle-hole symmetry breaking in the pseudogap state of Bi2201. *Nat. Phys.* **6,** 414 (2010).

30. R. A. Kaindl *et al.*, Ultrafast mid-infrared response of $YBa_2Cu_3O_{7-\delta}$. *Science* **287,** 470 (2000).

31. N. Gedik *et al.*, Single-quasiparticle stability and quasiparticle-pair decay in $YBa_2Cu_3O_{6.5}$. *Phys. Rev. B* **70,** 014504 (2004).

32. E. E. M. Chia *et al.*, Observation of competing order in a high-T_c superconductor using femtosecond optical pulses. *Phys. Rev. Lett.* **99,** 147008 (2007).

33. Y. H. Liu *et al.*, Direct observation of the coexistence of the pseudogap and superconducting quasiparticles in $Bi_2Sr_2CaCu_2O_{8+y}$ by time-resolved optical spectroscopy. *Phys. Rev. Lett.* **101,** 137003 (2008).

34. A. V. Fedorov *et al.*, Temperature dependent photoemission studies of optimally doped $Bi_2Sr_2CaCu_2O_8$. *Phys. Rev. Lett.* **82,** 2179 (1999).

35. That this is a bulk superconducting effect is corroborated by the magnetic field-dependent suppression of the Knight shift (a measure of the density of states at E_F) seen below T_c of Bi2201 in nuclear magnetic resonance (*36*). The Knight shift was found to drop sharply at T^*, exhibiting a similar temperature dependence as those shown in Fig. 3.

36. S. Kawasaki, C. Lin, P. L. Kuhns, A. P. Reyes, G.-q. Zheng, Carrier-concentration dependence of the pseudogap ground state of superconducting $Bi_2Sr_{2-x}La_xCuO_{6+\delta}$ revealed by $^{63,65}Cu$-nuclear magnetic resonance in very high magnetic fields. *Phys. Rev. Lett.* **105,** 137002 (2010).

37. S. V. Borisenko *et al.*, Two energy gaps and Fermi-surface "arcs" in $NbSe_2$. *Phys. Rev. Lett.* **102,** 166402 (2009).

Figure 1: Fermi surface maps measured below T_c at 10 K (left) and above T^* at 172 K (right) in the same momentum-space region (flipped for display). Dashed white lines labeled C1-C7 depict the cuts along which the EDCs shown in Fig. 2, A-N were measured. Purple dots labeled P1-P16 along M-Γ indicate momenta where EDCs in Fig. 2, V-W) were measured. Red and blue squares on the left indicate momenta of the Fermi crossing k_F (k_{F1} and k_{F2} in Fig. 2, A-G) at 172 K and back-bending k_G (black arrows in Fig. 2, O-S) at 10 K of the dispersion of the EDC maximum along cuts C1-C7. Red and blue circles on the right indicate momenta of identifiable peaks in the momentum distribution curves (measured along cuts parallel to Cut C7) at E_F at 172 K and 10 K, respectively. The solid red curves are a guide to the eye for the red squares and circles, whereas the dashed blue curve is the guide for the blue squares, together they show an increased $k_G - k_F$ misalignment going away from the nodal towards the antinodal region. The magenta-shaded region is approximately where multiple EDC features are found at 10 K (Figs. 2W and S2F).

Figure 2: (**A**)-(**G**) and (**H**)-(**N**) Selected EDCs at 172 K and at 10 K, respectively, for cuts C1-C7 approximately perpendicular to Γ-M (Fig. 1). Each EDC corresponds to a white point in the cuts in Fig. 1. EDCs in magenta and orange are located close to k_F. (**O**)-(**U**) Dispersions of the EDC features in (A)-(N) for cuts C1-C7. For each dispersion curve, every other symbol corresponds to an EDC in (A)-(N). Error bars are estimated based on the sharpness of features, to be ±3 meV minimum and ±8 meV maximum [examples shown in (O)] based on various EDC analyses (*27*). (**V**)-(**W**) EDCs at momenta P1-P16 along M-Γ (Fig. 1) at 172 K and 10 K, respectively. Circles denote the EDC shoulder feature (solid green), the EDC maximum feature at 10 K (blue) and at 172 K (red).

Figure 3: Temperature dependence of Kerr rotation (θ_K) measured by PKE, in comparison with that of the binding energy position of the EDC maximum at k_F given by ARPES (reproduced from Fig. S1F and Ref. (*29*)). ARPES results are normalized to the 80 K values. The dashed black curve is a guide to the eye for the PKE data, showing a mean-field-like critical behavior close to T^* (see additional discussion (*27*)). Left inset: Temperature dependence of the transient reflectivity change measured by TRR (right axis). The dashed black curve (left axis) is reproduced from the main panel. Error bars (if invisible) are smaller than the symbol size. Right inset: The dispersion of the EDC maximum at various temperatures above T_c, summarizing the results of Figs. 2A, S1F and 4A. Data were taken on samples from the same growth and annealing batch. The same growth batch but with different annealing was used in Ref. (*29*).

Figure 4: (**A**) and (**B**) Selected EDCs at 40 K and 22 K along Cut C1 (Fig. 1). See Fig. 2, A and H for data at 172 K and 10 K, Fig. S1, A-E for other intermediate temperatures. (**C**) Antinodal EDCs at 10 K after dividing by the 40 K counterparts, covering the momentum range indicated by the grey bar in (H), to be compared to those in (**D**) taken in a similar range at 30 K on an OP Bi2212 sample. Non-dispersive peaks are seen in both cases despite different sharpness and energy positions. (**E**)-(**G**) EDCs at different fixed momenta [specified in (A) and (H)] and temperatures around T_c. The counterintuitive increase above T_c of the antinodal gap defined by the EDC maximum in (F) and (G) reflects the existence of more than one energy scale below T_c. Insets: Corresponding EDCs divided by the 60 K counterpart, showing the peaks losing definition above T_c (Fig. S2E). (**H**) Summary for the dispersions of corresponding EDC features across and below T_c. Vertical arrows specify momenta M, k_{F2} at 172 K and k_{G2} at 10 K. Apparent asymmetry of the dispersions across M is due to a finite deviation of the cut from the high-symmetry direction and a subtle balance of spectral weight between different features in the EDC. All EDC features and error bars are similarly determined as in Fig. 2.

k_y

k_x

Γ

M

M

C1

C3

C5

C7

C2

C4

C6

P16

P1

High

Low

10 K
($<T_c$)

172 K
($>T^*$)
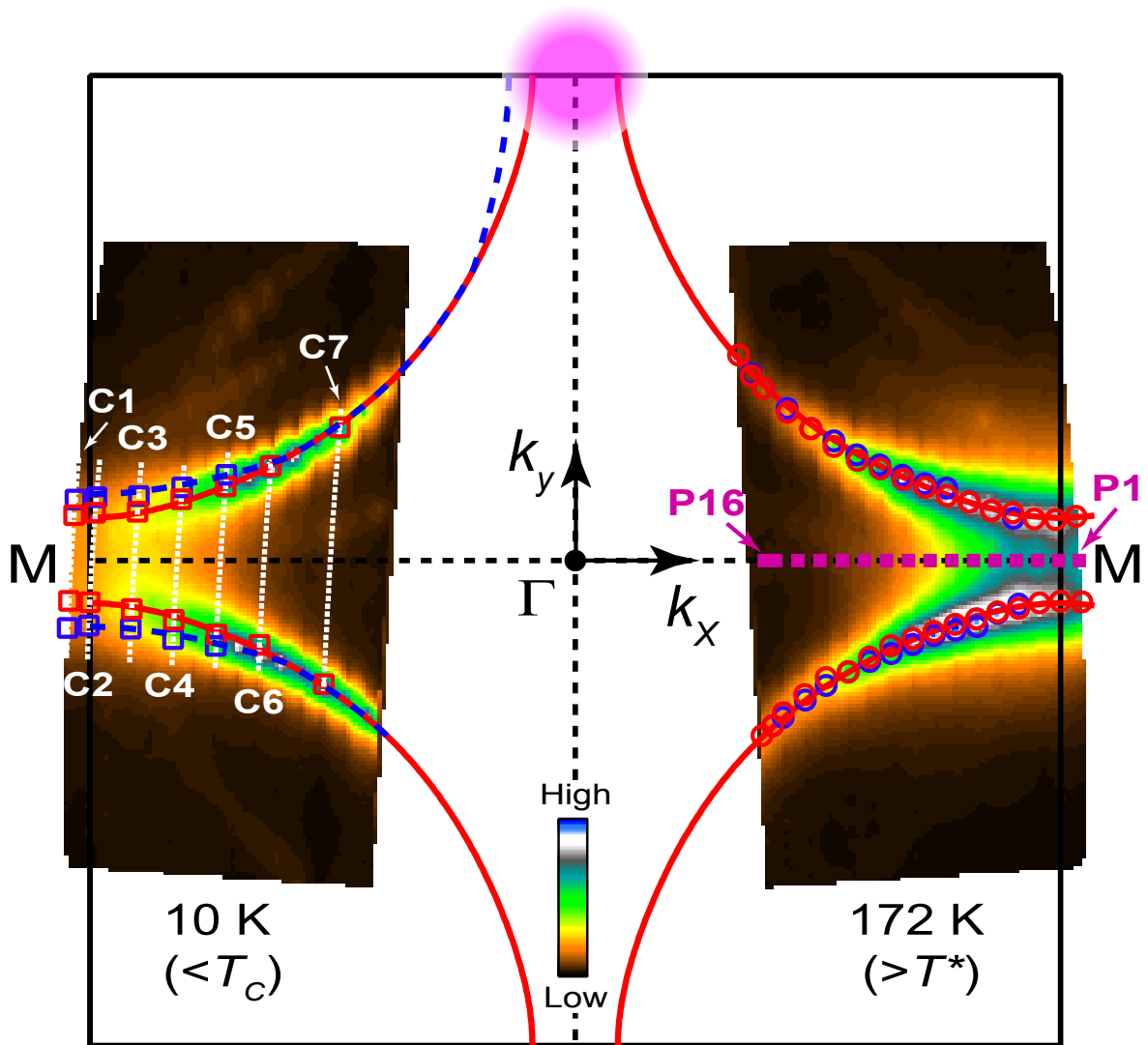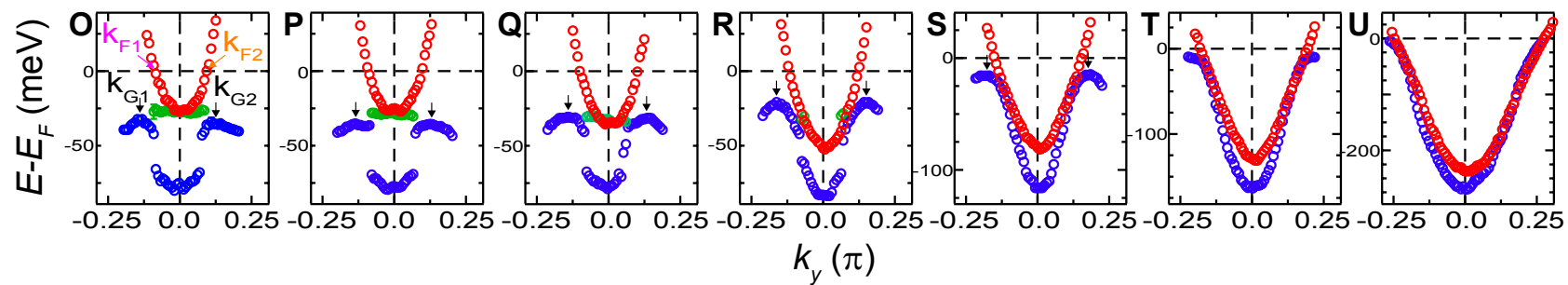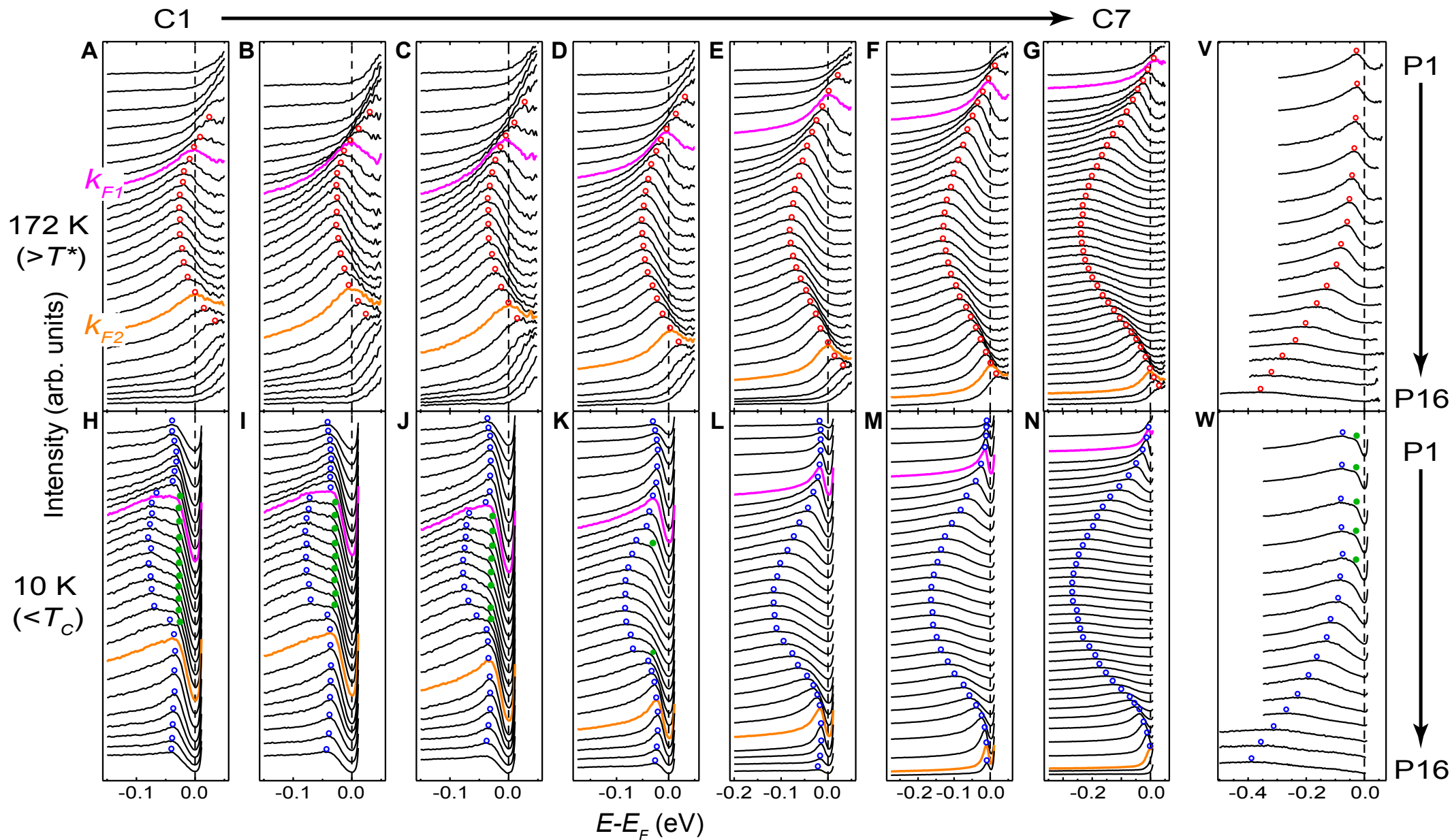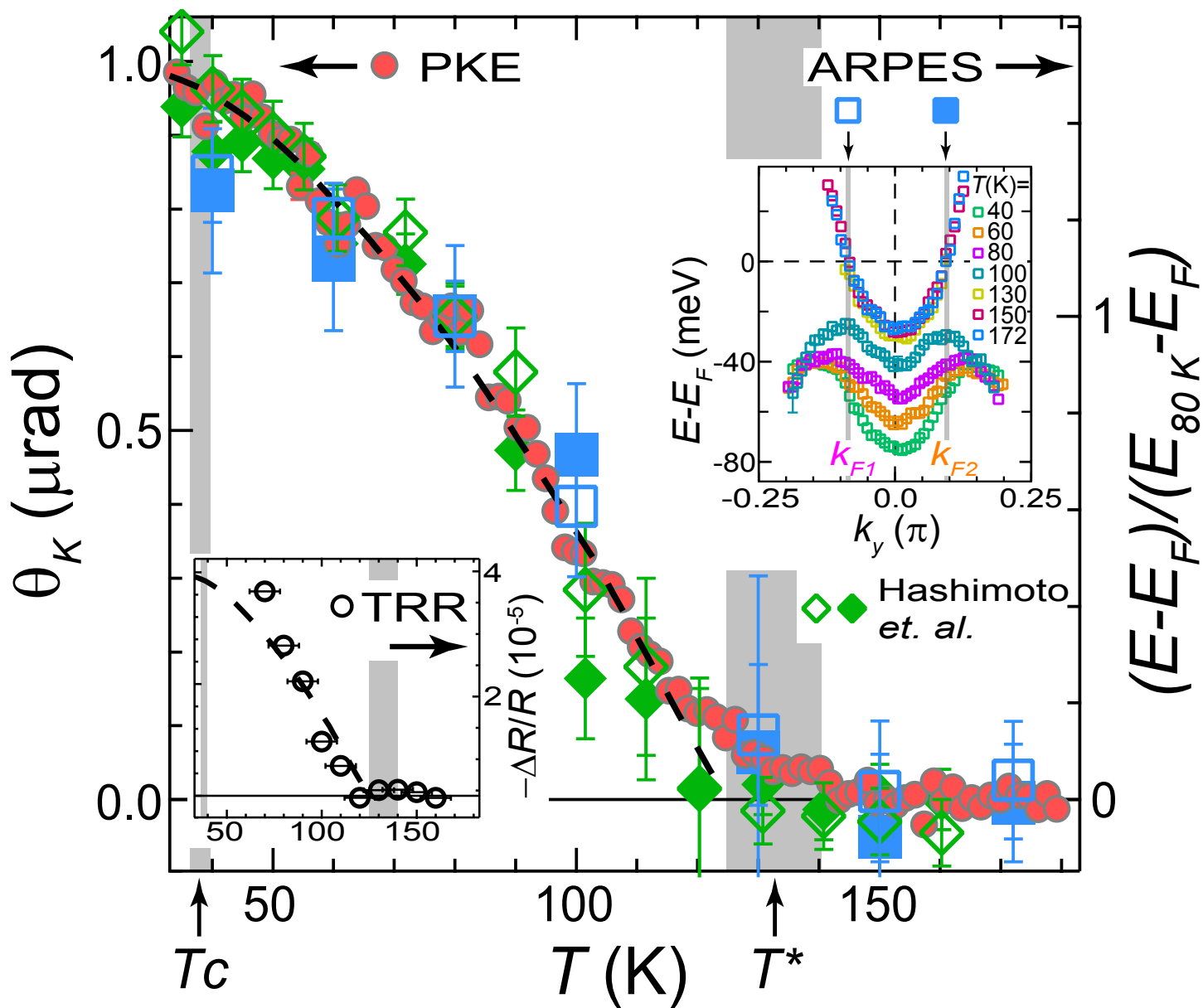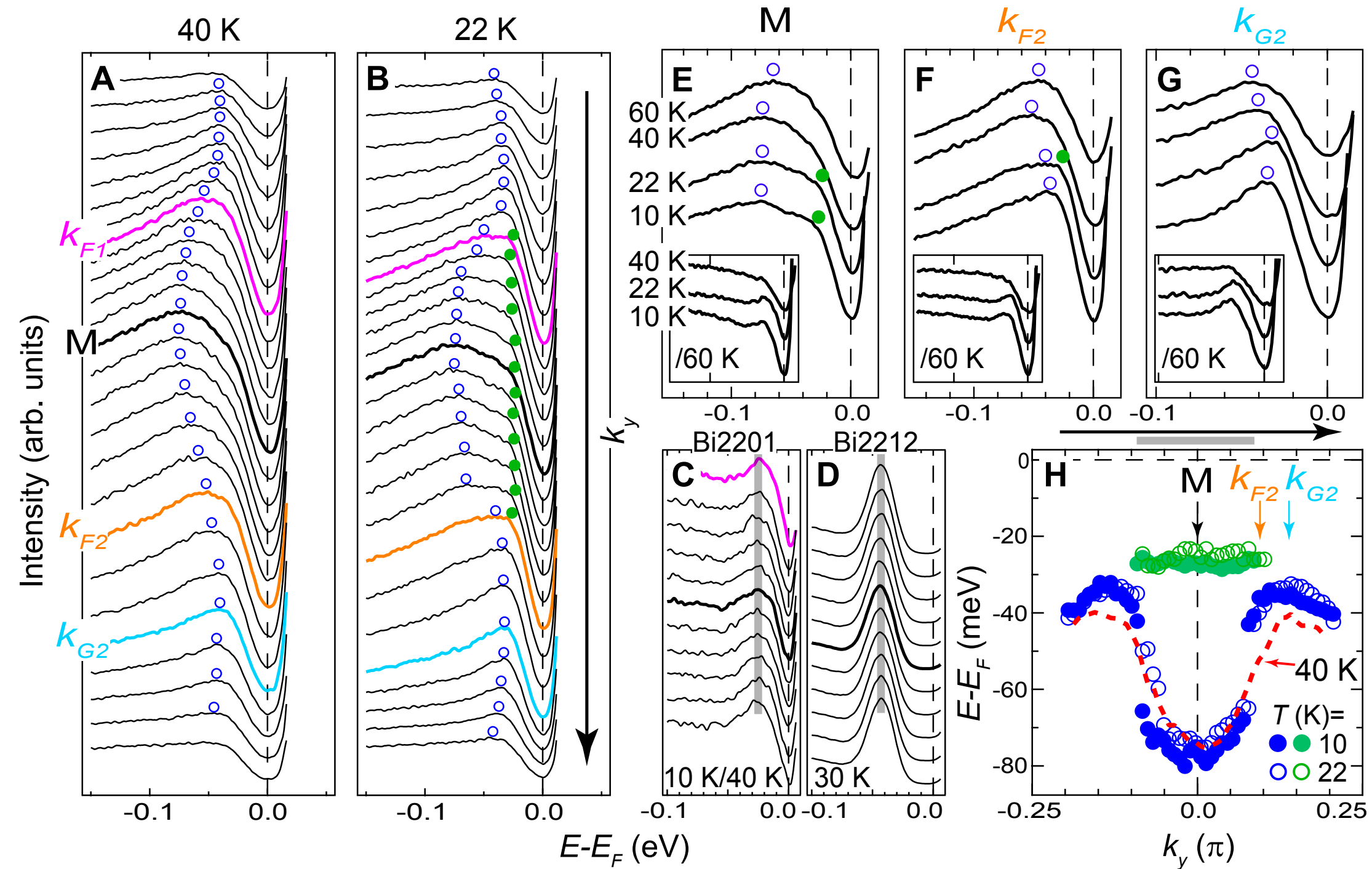
Supporting Online Material for
From a single-band metal to a high-temperature superconductor via two thermal phase transitions

Rui-Hua He,[1,2,3*] M. Hashimoto,[1,2,3*] H. Karapetyan,[1,2] J. D. Koralek,[3,4]
J. P. Hinton,[3,4] J. P. Testaud,[1,2,3] V. Nathan,[1,2] Y. Yoshida,[5] Hong Yao,[1,3,4]
K. Tanaka,[1,2,3,6] W. Meevasana,[1,2,7] R. G. Moore,[1,2] D. H. Lu,[1,2] S.-K. Mo,[3]
M. Ishikado,[8] H. Eisaki,[5] Z. Hussain,[3] T. P. Devereaux,[1,2†]
S. A. Kivelson,[1†] J. Orenstein,[3,4†] A. Kapitulnik,[1,2†] Z.-X. Shen[1,2†]

Contents

1 Materials and Methods

1.1 Samples

High-quality single crystals of $Pb_{0.55}Bi_{1.5}Sr_{1.6}La_{0.4}CuO_{6+\delta}$ (Pb-Bi2201) and

$Bi_{2-x}Pb_xSr_2CaCu_2O_{8+\delta}$ (Pb-Bi2212) near optimal doping were grown by the travelling-solvent floating zone method. The Pb doping suppresses the super-modulation in the BiO plane and min-imizes complications in the electronic structure due to photoelectron diffraction. The carrier con-centrations of the samples were carefully adjusted by a post-annealing procedure under flowing N_2 gas which varies the oxygen content, and were estimated from the Fermi surface volumes, e.g., for Pb-Bi2201 shown in Fig. 1 to be ~ 25.3 %, which is consistent with previous reports for near optimal doping (*S1, S2, S3*). X-ray and Laue diffraction showed no trace of impurity phases. For Pb-Bi2201, the onset temperature of the superconducting transition, T_c, determined by SQUID magnetometry, was 38 K, with a resistive transition width less than 3 K ($T_c = 97 \pm 2$ K for Bi2212 related to Fig. 4D); the pseudogap temperature, $T^* = 132$ K ± 8 K, is determined based on the observed closing of the antinodal pseudogap in ARPES (Fig. S1F), which coincides within exper-imental uncertainty with the onset of Kerr signal in PKE and that of transient reflectivity in TRR

2

(Fig. 3). This T^* value is also consistent with our resistivity measurement on the same crystals as well as other reports of different measurements on Bi2201 near optimal doping (*S3, S4, S5, S6, S7*). We found T^* depends more sensitively on the post-annealing condition than T_c near optimal doping but remains consistent among samples within the same growth and post-annealing batch.

1.2   Measurements

1.2.1   ARPES

Angle-resolved photoemission spectroscopy (ARPES) measurements were performed at Beamline 5-4 of the Stanford Synchrotron Radiation Lightsource (SSRL) with a SCIENTA R4000 electron analyzer. Preliminary photon energy and polarization dependent ARPES measurements were performed at Beamline 10.0.1 of the Advanced Light Source (ALS). All presented data were taken using 22.7 eV photons mainly in the first Brillouin zones with total energy and angular (momentum) resolutions of $\sim$ 10 meV and $\sim 0.25°$ ($\sim 0.0096\text{Å}^{-1}$), respectively. The temperatures were recorded closest to the sample surface position within an accuracy $\pm$ 2 K. The samples were cleaved and measured in an ultra high vacuum chamber with a base pressure of better than 3×10^{-11} Torr which was maintained below 5×10^{-11} Torr during the temperature cycling. Measurements on each sample were completed within 48 hours after cleaving. All data shown in the main text were obtained on the same sample and were reproduced on different samples from the same batch with sample cleaving at low (10 K) or high ($\sim$ 150 K) temperature. The possibility of sample aging in each experiment was excluded by monitoring the nodal dispersion without complications by the gap opening. A similar experimental routine has been previously demonstrated and detailed in the supplementary information of Ref. (*S3*).

1.2.2   Polar Kerr effect

Polar Kerr effect (PKE) measurements were performed using a zero-area-loop Sagnac interferometer at a wavelength of $\lambda = 1550$ nm, spot size of $\sim 3\mu$m, and sensitivity of 0.1 μrad/$\sqrt{Hz}$ at 250

μW of incident optical power (*S8*). In its used configuration, the apparatus was sensitive to only the polar Kerr effect, hence to any ferromagnetic component of the local magnetization, perpendicular to the plane of incidence of the light. The same apparatus was previously used to detect the effect of time-reversal symmetry breaking below T_c in Sr_2RuO_4 (*S9*) and in the vicinity of T^* in $YBa_2Cu_3O_{6+x}$ (YBCO) (*S10*).

For YBCO, measurements on crystals with various doping levels revealed a sharp phase transition at a temperature T_s(p) below which there is a non-zero Kerr rotation. Both the magnitude and doping dependence of T_s were found to be in close correspondence with T^* which has been identified in other physical quantities. In particular, T_s is substantially larger than T_c in underdoped materials, but drops rapidly with increasing doping, so that it is smaller than T_c in a near optimally-doped crystal and extrapolates to zero at a putative quantum critical point under the superconducting dome. The magnitude of the Kerr rotation in YBCO is smaller by ~ 4 to 5 orders of magnitude than that observed in other itinerant ferromagnetic oxides, suggesting that at most it measures a very small "ferromagnetic-like" component of a magnetic transition. However, the temperature dependence of the PKE near T_s, together with complementary measurements using other probes, strongly suggest that the PKE tracks a secondary order parameter which is driven by another transition that is not necessarily magnetic. Corroborating evidence in that direction comes from neutron measurements on x= 0.45 (*S11*) finding evidence for a nematic state in this composition, and from muon-spin-rotation measurements indicating charge ordering transition (*S12*) near optimal doping. Interpolating between these two ends which find T^* that agrees with the PKE measurements, we speculate that the PKE tracks an electronic transition that may evolve smoothly from strong charge ordering to a weaker nematic phase.

While the above discussion on YBCO relies on circumstantial evidence, the present results on Pb-Bi2201 may be the first unambiguous data that suggests that T^* can be identified, which corresponds to a true symmetry-breaking transition and the primary order parameter that governs

that transition is electronic.

1.2.3 Time-resolved reflectivity

Time-resolved reflectivity (TRR) measurements were performed using a 100 MHz mode locked Ti: Sapphire oscillator operating at a wavelength of 800 nm. In these measurements, femtosecond (fs) pulses of linearly-polarized light excite the sample, and time (t)-delayed probe pulses from the same laser measure the resulting change in reflectivity, ΔR. In the present context, the power of this technique lies in its ability to distinguish different phases by their response dynamics. Fig. S3 shows TRR data taken on Pb-Bi2201 at 3 different pump powers with a focal spot diameter of roughly 100 μm. The grey and pink shaded regions highlight the pseudogap and superconducting responses, respectively. As discussed in the main text, the superconducting signal, seen in Fig. S3B & C, is attributed to the breaking of Cooper pairs, and its temperature and pump-fluence dependence are consistent with previous work (*S13*). It is characterized by a positive signal which decays on the picosecond (ps) time scale. The pseudogap signal, on the other hand, is centered about zero delay and decays on the 100 fs timescale. The pseudogap signal is generally weaker than the superconducting one and becomes more pronounced with increasing pump power. However, the average heating of the sample becomes significant at low temperatures for high pump powers, which can almost completely suppress the superconducting response. The magnitude of the negative TRR signal in the left inset of Fig. 3 is extracted from the 15 mW data (Fig. S3A) by taking the difference between the maximum for $t < 0$ and the minimum near $t = 0$. Because of the laser heating at this power, we only show the data for $T \geq 25$ K, and estimate an error bar of ± 8K for the actual sample temperature.

1.3 ARPES data analysis

To remove the effect due to cutoff by the Fermi-Dirac (FD) function, raw ARPES spectra have been divided by a convolution of the FD function at the given temperature and a Gaussian with its

width fixed at the energy resolution. Note that this division is an approximation for the complicated deconvolution that aims at removing the energy resolution effect. It works well for high temperatures when the overall width of FD function ($\sim 4k_BT$) is much larger than the energy resolution and becomes bad for low temperatures. This procedure allows us to recover the actual band dispersions closest to E_F and trace them above E_F at high temperatures, when thermal population leads to appreciable spectral weight. It is also necessary for revealing that the EDC shoulder feature at low temperatures is not trivially produced by the Fermi cutoff. Because the uncertainty introduced by the division to the spectral line shape is limited to ~ 4 meV ($= 4k_BT$) at 10 K around E_F, the discussed low-temperature spectral evolution across T_c for features (such as the EDC shoulder feature) located beyond this E_F vicinity remains robust. The faithfulness of this procedure can be reflected by the observations after the division that the EDC shoulder feature at low temperatures does not show up everywhere but is confined in the antinodal region and that the nodal Fermi crossings are recovered at all temperatures. However, one should exercise caution when associating the gap function at low temperatures directly with the peak position of the FD-divided spectrum (Fig. S4), particularly in the vicinity of the node where the gap is intrinsically small.

The subsequent EDC analysis was performed on the FD-divided spectra: the EDC maximum below E_F is identified by taking the first derivative of the moderately-smoothed EDC (w.r.t. the energy axis); suspected additional features below E_F and local maxima above E_F are estimated based on the first derivative and aided with eyeball correction; the (non-)existence and energy position of the EDC shoulder feature are determined mainly based on a spectral subtraction analysis (Fig. S2), which is in general consistence with the spectral division method using 40 K data (Fig. 4C) and with eyeball estimates.

2 Simulations

2.1 Simple density-wave pseudogap order

We describe modifications of the band structure due to d-wave superconductivity (Fig. S7B & F) and its coexistence with some long-range density wave order of wave vector q (Fig. S7C, D, G & H) in a simple mean-field approach, modified from what we previously used in Ref. (*S3*). We confine the use of this approach only to low temperatures, where order parameter fluctuations are less severe and thus a simple mean-field description of the data might have a better chance of success.

The mean-field coexistence Hamiltonian is given by: $H = \sum_k \epsilon_k c_k^\dagger c_k + \sum_{k,q} V_q (c_{k+q}^\dagger c_k + h.c.) + \sum_k \Delta_k (c_{k\uparrow}^\dagger c_{-k\downarrow}^\dagger + h.c.)$, where V_q and Δ_k are the density wave and superconducting order parameters, respectively; $c_k^\dagger (c_k)$ is the creation (annihilation) operators for electrons at k. $\varepsilon_k = -2t(\cos k_x + \cos k_y) - 4t' \cos k_x \cos k_y - 2t''(\cos 2k_x + \cos 2k_y) - 4t'''(\cos 2k_x \cos k_y + \cos k_x \cos 2k_y) - \varepsilon_0$, where $t, t', t'', t''', \varepsilon_0 = 0.22, -0.034315, 0.035977, -0.0071637, -0.24327$ eV, respectively, is the tight-binding bare band dispersion which is obtained by a global fit to the experimental EDC dispersions at 172 K (Fig. S5).

We consider in the following only the density wave orders with generic qs that largely connect the antinodal portion (rather than the nodal one) of the Fermi surface, where the particle-hole asymmetry of spectra is the strongest.

In case of bond-diagonal density wave order with a commensurate $q = q_{AF} = [\pi, \pi]$, the eigenstate $|\psi_k\rangle = u_k |k\rangle + u_{k+q_{AF}} |k+q_{AF}\rangle + u_{-k} |-k\rangle + u_{-k-q_{AF}} |-k-q_{AF}\rangle$ for the Hamiltonian with the eigenenergy $\varepsilon'(k)$ can be obtained by solving the matrix $M_{AF+SC} = \begin{bmatrix} A_{AF} & D_{SC} \\ D_{SC} & -A_{AF} \end{bmatrix}$, where $A_{AF} = \begin{bmatrix} \varepsilon_k & V_2 \\ V_2 & \varepsilon_{k+q_{AF}} \end{bmatrix}, D_{SC} = \Delta I, I$ is a 2×2 identity matrix. We expect this case to generically represent density wave orders of q approximately along the bond-diagonal direction, such as d-density wave, antiferromagnetic order with $q = q_{AF}$ and incommensurate spin stripes

with a finite, small deviation of q away from q_{AF}.

In case of bond-direction density wave order, we consider the checkerboard case with $q_1 = [0.15\pi, 0]$ and $q_2 = [0, 0.15\pi]$, $M_{CB+SC} = \begin{bmatrix} A_{CB} & D_{SC} \\ D_{SC} & -A_{CB} \end{bmatrix}$, where $D_{SC} = \Delta I$, $A_{CB}(I)$ are all 1600×1600 (identity) matrices. A_{CB} is determined by the following, base: $\{k + mq_1 + nq_2; m, n = 0, ..., N-1; N = 200/gcd(2*100, 0.15*100) = 40\}$; matrix element: $A_{CB}(m, n; m', n') = V_1$, only if $|m - m'| + |n - n'| = 1$ or $(|m - m'| + |n - n' - N + 1|)(|m - m' - N + 1| + |n - n'|) = 0$ [with small high-order interaction neglected (*S14*)], and 0 otherwise. Eigenstate is thus $|\psi_k\rangle = \sum_{m,n} u_{k+mq_1+nq_2}|k + mq_1 + nq_2\rangle + u_{-k-mq_1-nq_2}|-k - mq_1 - nq_2\rangle$. Superposition of two orthogonal stripe orders with q_1 and q_2 gives overall similar results as the checkerboard case.

Several key aspects of our experimental observations (Fig. S7A & E) are qualitatively reproduced in both these cases. In the nodal region, a single dominant branch opens up a d-wave gap along the underlying Fermi surface (Fig. S7E-H and the insets). In contrast, multiple branches of comparable spectral weight are seen in the antinodal region, with one branch exhibiting little dispersion in two dimensions and another dispersive branch which shows back-bending at k_G away from k_F.

2.2 Pair-density-wave pseudogap order

Other density-wave alternatives for the broken-symmetry pseudogap order have not been (but should be) explored. A particularly interesting candidate is the pair density wave order, as an inherent mixture of density-wave and superconducting correlations (*S15, S16, S17*).

2.3 Simple nematic pseudogap order

Nematic order, which breaks rotational symmetry but not translational symmetry of the lattice can also potentially explain our key observations in the superconducting state. We have studied a simple form of a nematic distortion (Pomeranchuk type) of the bare Fermi surface that introduces a difference in t for the x and y directions, $t_y = \alpha t_x$ but not in t', t'', t''' (ε_0 is ad-

justed to maintain the Luttinger's volume). α is chosen so that the experimental k_G falls on the distorted Fermi surface and the superconducting gap opens along the distorted Fermi surface (inset of Fig. S8D). The tight-binding parameters are chosen to be $t_x, t', t'', t''', \varepsilon_0$ & $\alpha =$ 0.22, -0.034315, 0.035977, -0.0071637, -0.24127 eV & 1.0989.

Two types of orthogonal domains exist in a tetragonal crystal. ARPES is expected to detect a superposition of signals from both domains which gives rise to an apparent two-band band structure as shown in Fig. S8A. The onset of superconductivity produces a gap for each band (Fig. S8B). Consistent with the experiment, two band features, one dispersionless and the other dispersive showing back-bending, are seen in the antinodal region (Fig. S8C). But two bands can still be seen away from this region (Fig. S8D), in contrast with what is seen in experiment. However, one should note that an energy-dependent broadening could in principle make two bands appear to be one when they are close enough. Where the two bands are farthest apart in the antinodal region, an increased coherence of the low-energy band at low temperatures could allow two features to be separately resolved.

2.4 Pitfalls

Although these mean-field results present a favorable zeroth-order consistency with the experiment, it is important to point out that they also fail to capture other important aspects of the data. Most obviously, in mean-field theory the quasiparticles are exact eigenstates which produce sharp spectral features; this contrasts with the broad features seen in experiment, e.g., cf. Fig. S7I-J near the M point. We have tried to correct this by including a phenomenological broadening (described below) but this still does not adequately reproduce the data (see the caption of Fig. S7). These discrepancies probably reflect the effects of finite correlation length (*S3*) and strong electron correlations.

2.5 Quasiparticle lifetime broadening introduced to the simulations

All simulation results, except those in Figs. S6 & S7K, are shown with the renormalized band dispersion $\varepsilon'(k)$ broadened by a Fermi-liquid-like energy-dependent linewidth $\Gamma = 0.1\omega^2 + 0.005$ (eV) and its intensity proportional to $|u_k|^2$. Fig. S7K assumes a phenomenological (marginal-Fermi-liquid-like) spectral function with a linewidth, $\Gamma = \sqrt{(\alpha\omega)^2 + (\beta T)^2}$ (eV), where $\alpha =$0.715 and $\beta =$2.57. This model was demonstrated to provide a reasonable global fit to the experimental antinodal spectra of heavily-overdoped Bi2212 ($T_c=$ 65 K) taken at various photon energies (16.6 - 32 eV) within energy (-200 - 50 meV) and temperature (10 - 128 K) ranges comparable to our study (*S18*).

2.6 Effects of finite experimental resolutions and quasiparticle lifetime

The ARPES simulation in Fig. 6 is based on a phenomenological spectral function in the superconducting state (*S19*). We use the same global tight-binding bare band structure and assume d-wave superconductivity ($\Delta = 35$ meV). The experimental energy and momentum resolutions and a realistic quasiparticle linewidth ($\alpha =$0.715 and $\beta =$2.57) are incorporated. We find that these factors have a negligible effect on the $k_G - k_F$ misalignment.

3 Additional discussion

3.1 On the nature of the broken-symmetry pseudogap state

An outstanding task after presenting our data in the main text is to identify the nature of the broken-symmetry state, and to relate it to the apparently similar electronic changes that occur below T^* in other cuprates. There are two real-world considerations which complicate this program: **1)** To the extent that the pseudogap state involves broken spatial symmetries, the role of quenched disorder is typically severe. It is expected to round the transition and to limit the growth of the pertinent correlations below T^* to a limiting length scale which diverges only as the strength of the disorder

tends to zero. This means that macroscopic measures of broken symmetry, especially where (as in Bi2201) the dopant atom distribution produces an inescapable degree of randomness, are expected to be less precise than they are in idealized models. **2)** In comparing different materials, even if the same "universal" physics underlies the pseudogap, there can be detailed material-specific differences, even in the precise patterns of broken symmetry involved, making cross-material comparisons more subtle than they would be in idealized models.

While nominally the onset of PKE at T^* suggests that the pseudogap phase uniformly breaks time-reversal symmetry, the small size of the effect and the lack of any directly detectable ferromagnetism below T^* make this conclusion uncertain, as previously discussed in the case of YBCO (*S10*). A recent zero-field nuclear magnetic resonance (NMR) study detected no static magnetism on the Cu sites in superconducting Bi2201 (*S20*), implying that either the magnetism has a very novel character (*S21, S22*) or that there is no magnetism. In either case, the similarity of the PKE onset at T^* in Bi2201 and YBCO supports the proposition that the pseudogap order has a common character in a broad class of cuprate superconductors.

The large magnitude of the antinodal gap ($\sim 3.5 k_B T^*$, measured relative to E_F) at temperatures well below T^* and the fact that it removes a substantial portion of the Fermi surface, implies that the spectral changes detected in ARPES reflect the primary pseudogap order. This is consistent with what has been inferred from the temperature dependence of the Knight shift measured by NMR (*S20*) of bulk Bi2201 in high enough magnetic fields to suppress superconductivity: The density of states (DOS) at E_F begins to drop sharply at T^*, exhibiting a similar temperature dependence as those shown in Fig. 3. However, also consistent with the ARPES, a substantial fraction of the DOS remains ungapped down to 0 K.

3.2 Implications with various reported candidates for the pseudogap order

Here we briefly compare the present results with studies of putative pseudogap order in other cuprate superconductors. Strong evidence has been found of nematic order in YBCO (*S11, S23*)

and Bi2212 (*S24, S25*). Evidence of unconventional translation-symmetry-preserving antiferromagnetism in YBCO (*S26*) and $HgBa_2CuO_{4+\delta}$ (*S27*) has also been reported. These experiments suggest the pseudogap may primarily involve a subtle form of discrete symmetry-breaking with the wave vector $\vec{Q} = 0$. While such order could produce significant shifts in the electron dispersion, without breaking translational symmetry (or particle conservation), however, it is hard to see, at least at mean-field level, how it would lead to a gap in the spectrum. There is substantial evidence of unidirectional spin and charge density wave order (*S28*) in various cuprates, which spontaneously break lattice translational symmetry. Such order could readily lead to the opening of a gap on the nested portions of the Fermi surface. However, direct evidence of the existence of such a state has been found by neutron and X-ray scattering experiments only at temperatures below $50 \sim 60$ K (well below T^*) in particularly "stripe-friendly" materials. Unless the order parameter is somehow anomalously difficult to observe in diffraction (*S21*), it is hard to believe that similar experiments would not have already seen new Bragg peaks in the pseudogap regime of many cuprates.

3.3 On the ordering vector of a putative density-wave pseudogap order

Ideally, by analyzing the momentum dependence of the spectral changes in ARPES spectra induced by the pseudogap, one might be able to back out information concerning the nature of the pseudogap order, such as the ordering vector, $\vec{Q}$, of a putative density-wave state. In mean-field theory, starting from a bare band structure, $\epsilon_{\vec{k}}$, as the temperature T is reduced below T^*, the pseudogap-induced spectral shifts would be expected to grow in proportion to $(T^* - T)^\beta$ with $\beta = 1/2$ only at special points in $\vec{k}$ space for which $\epsilon_{\vec{k}} = \epsilon_{\vec{k}-\vec{Q}}$. In all other cases such shifts would be proportional to $(T^* - T)^{2\beta}/|\epsilon_{\vec{k}} - \epsilon_{\vec{k}-\vec{Q}}|$. From Fig. 3, to the extent that the spectral shift at k_F and the change of Kerr rotation near T^* can be associated with a critical exponent, they are both proportional to $(T^* - T)^{2\beta}$ with $\beta \approx 1/2$. The former is thus consistent with the mean-field expectation for a poor nesting of the antinodal portion of Fermi surface, which is in turn supported by

the observed $k_G - k_F$ misalignment. A nematic order with $\vec{Q} = 0$ expects a scaling of $(T^* - T)^\beta$, which seems not quite consistent with this particular aspect of our data.

Although $\vec{Q}(\neq 0)$ can in principle be determined by studying the critical exponent as a function of position along the Fermi surface, there is every reason to think that order parameter fluctuations will significantly broaden both the temperature and momentum dependences of the spectroscopic signatures of the transition (even when the transition itself characterized by transport measurements remains sharp). Moreover, although the bare electronic structure is simple, its strange-metal nature precludes a safe description in terms of non-interacting quasiparticles with dispersion $\epsilon_{\vec{k}}$.
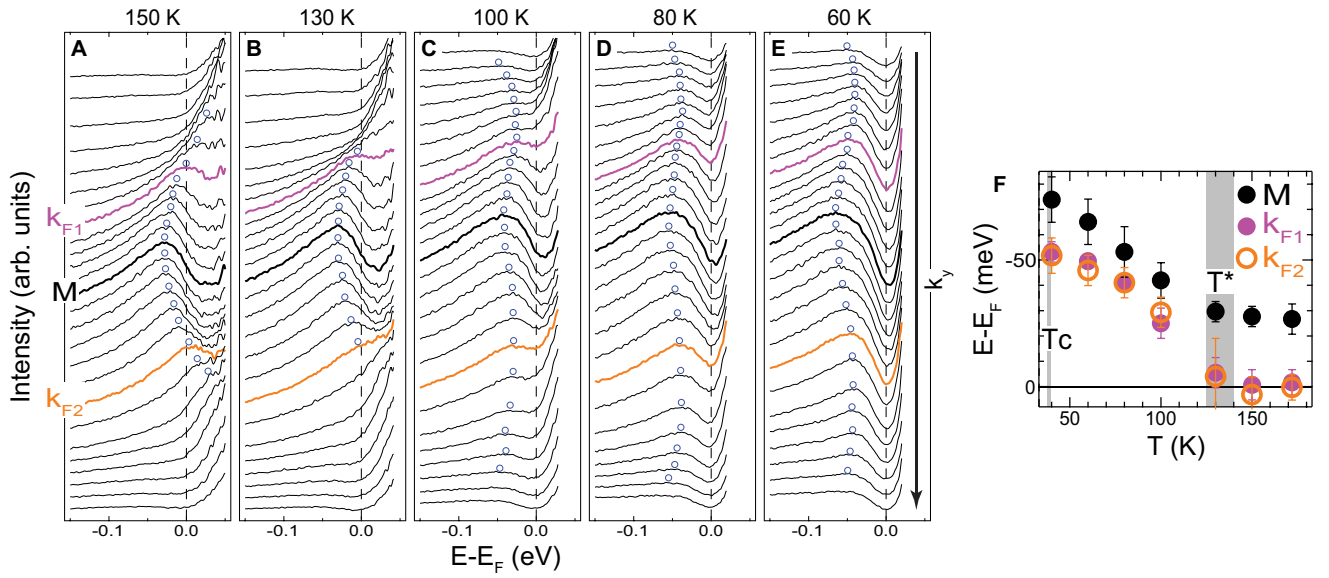
Figure S 1: **ARPES temperature dependence across** T^* **A-E,** Selected EDCs at five representative temperatures along Cut C1 shown in Fig. 1. The single EDC maximum is tracked to give the band dispersion summarized in the right inset of Fig. 3. **F,** Summary for the temperature-dependent binding energy position of the EDC maximum at M, k_{F1} and k_{F2}. Error bars are estimated based on the sharpness of features.
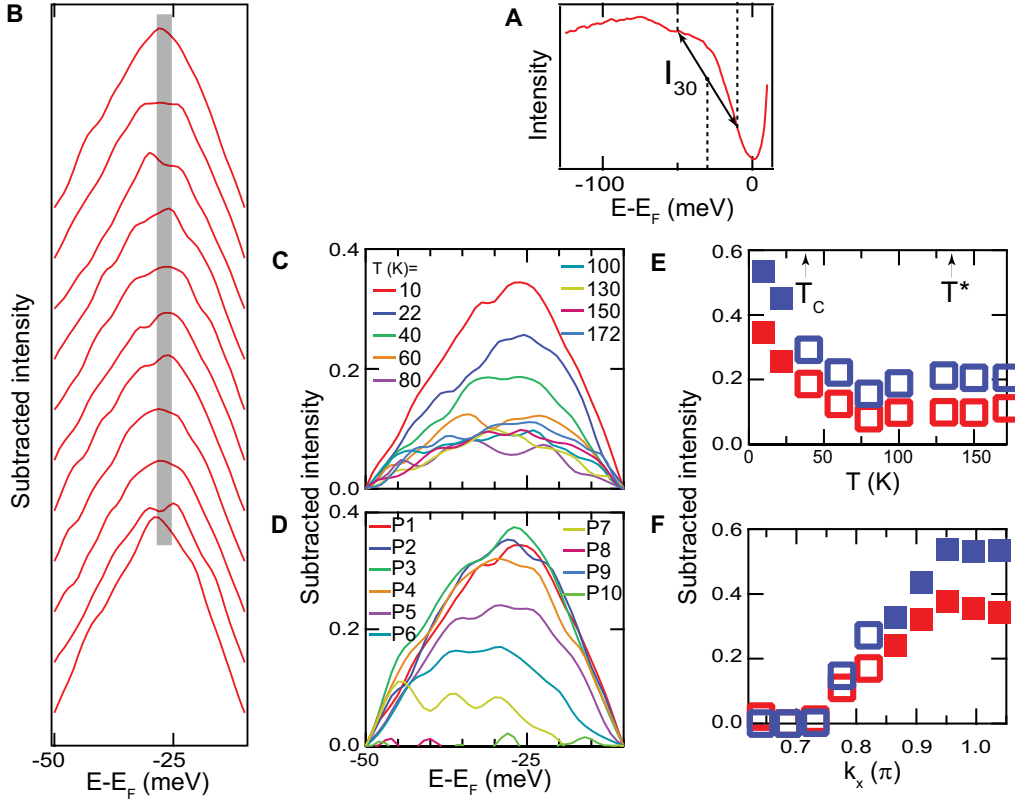
14

Figure S 2: **Determination of the EDC shoulder feature by spectral subtraction.** Subtraction was made for each EDC (e.g., the EDC at M at 10 K of Cut C1 as shown in **A**) by assuming a linear background connecting intensity at E_{i1}=-50 meV and E_{i2}=-10 meV. Intensity was then normalized by the linear intensity (I_{30}) at E_i=-30 meV. The subtracted EDCs show a clear intensity maximum from which we define the position of the original EDC shoulder. This method yields a similarly non-dispersive peak at a similar energy position as the spectral division using the 40 K data (e.g., as shown in **B** for the same data set as in Fig. 4C). It also provides a convenient way to quantify the temperature- and momentum-dependent existence of the EDC shoulder feature. **C** shows the subtracted EDCs (**A**) at various temperatures and **E** plots the temperature dependence of the maximum intensity (red) in comparison to a different subtraction using E_{i1}=-60 meV and E_{i2}=0 meV (blue). **D & F** show the results for P1-P10 (in Fig. 2W). We defined phenomenologically the threshold for existence of the EDC shoulder feature at the half-drop positions of the maximum intensity w.r.t. the background (solid/empty symbols for existence/non-existence in **E & F**). This consistently supports the eyeball estimate that the EDC shoulder feature loses its clear definition above T_c and beyond the antinodal region (along Γ-M). Note that its existence perpendicular to Γ-M could in principle extend wider than where is currently identified by green circles (Fig. 2O-R), due to its potential mixing with the EDC maximum feature near back-bending. Also note that the non-vanishing variation of the maximum intensity above T_c in **E** is consistent with the idea that superconducting fluctuations persist above T_c but still well below T^*, in nearly OP Bi2201 (*S29*) and other cuprates (*S30, S31*).
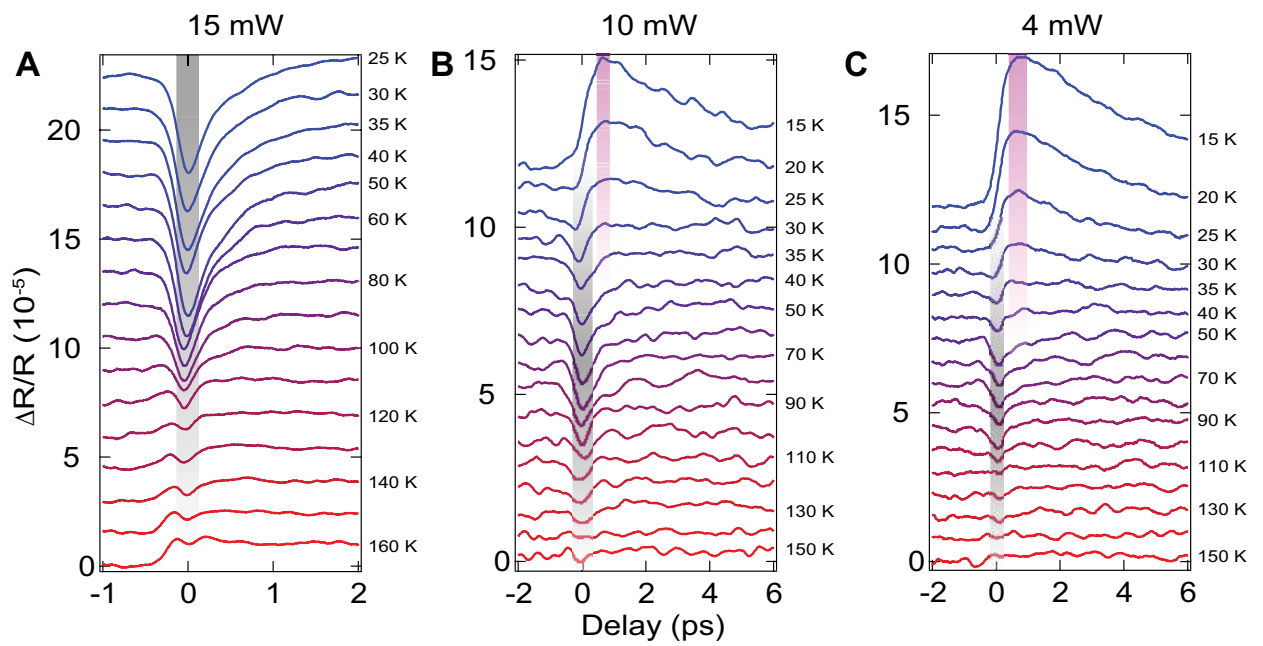
15

Figure S 3: **Temperature dependence of time-resolved reflectivity.** Results are shown at different laser powers, **A** 15 mW, **B** 10 mW, and **C** 4 mW. The grey and pink shaded regions highlight the pseudogap and superconducting responses respectively. Note that the 15 mW data was taken over a shorter delay range than the lower power data.
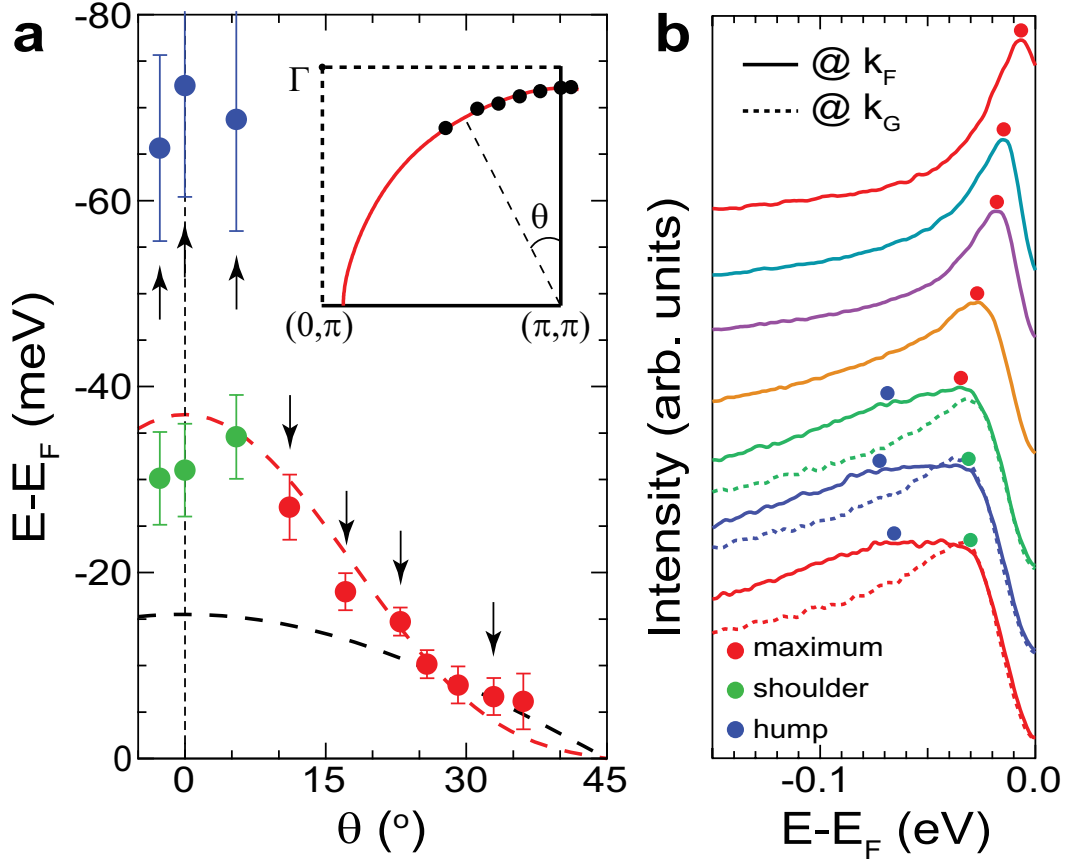
16

Figure S 4: **Gap function along the underlying Fermi surface at 10 K. A**, Binding energy positions of various spectral features in the EDCs at k_F plotted as a function of the Fermi surface angle. Red dashed curve is the gap function reported for OP Pb-Bi2201 (*S32*). Black dashed curve is a guide to the eye for a simple d-wave gap function. Our observation of multiple EDC features of comparable spectral weight in the antinodal region highlights the essential physics that eluded previous revelation. **B**, Selected EDCs at k_F (k_{F1}) as indicated by black arrows (dots) in (the inset of) **A**. The maximum feature is defined for EDCs with a single component seen away from the antinodal region. Both the shoulder at low energy and the hump at high energy are defined for EDCs at k_F in the antinodal region. The (antinodal) EDCs at the neighboring k_G (k_{G1}) are shown in dashed curves, which have a single component, reminiscent of those used to define the gap function in the antinodal region in many previous studies.
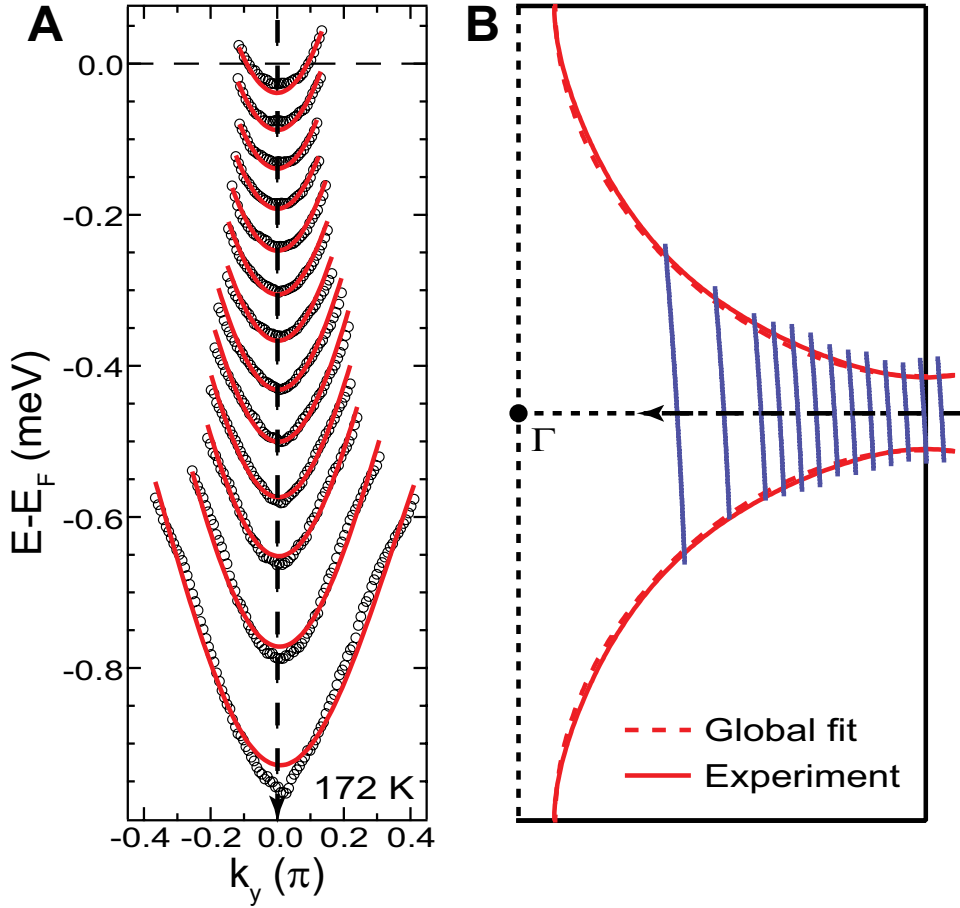
17

Figure S 5: **Global tight-binding fit. A**, Global tight-binding fit (red curves) to the EDC dispersions at 172 K (black circles) whose momentum loci are indicated by blue lines in **B**. For clarity, adjacent cut has a 50 meV relative vertical offset. Because of the global constraint, the fit gives a slightly larger ($\sim$ 7 meV) band bottom at M point than the experiment. **B** shows that the Fermi surface given by the global fit coincides with the experimental one reproduced from Fig. 1.
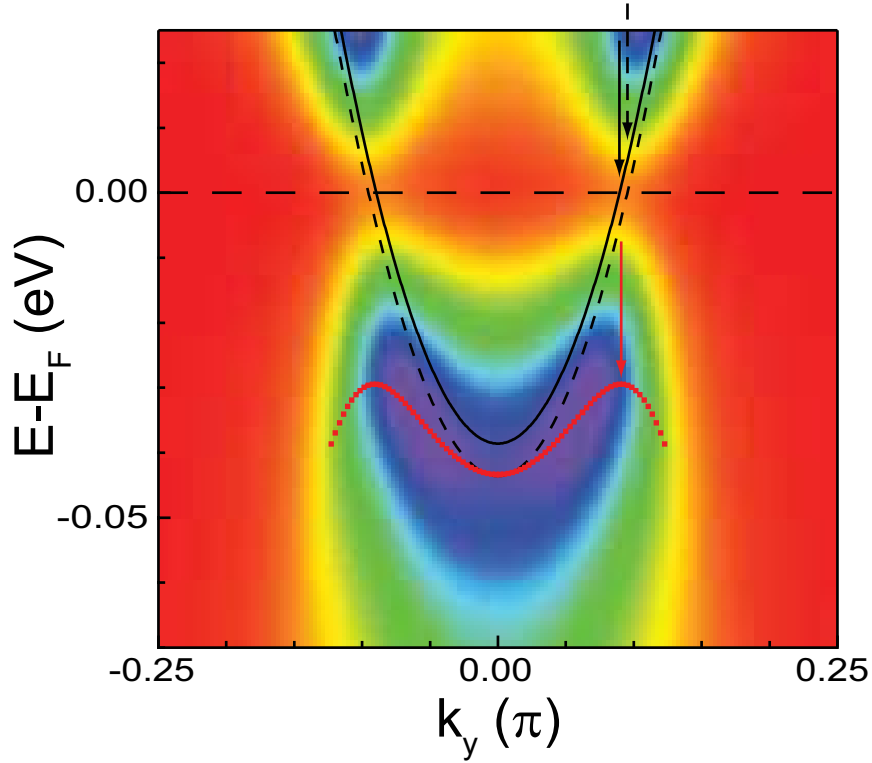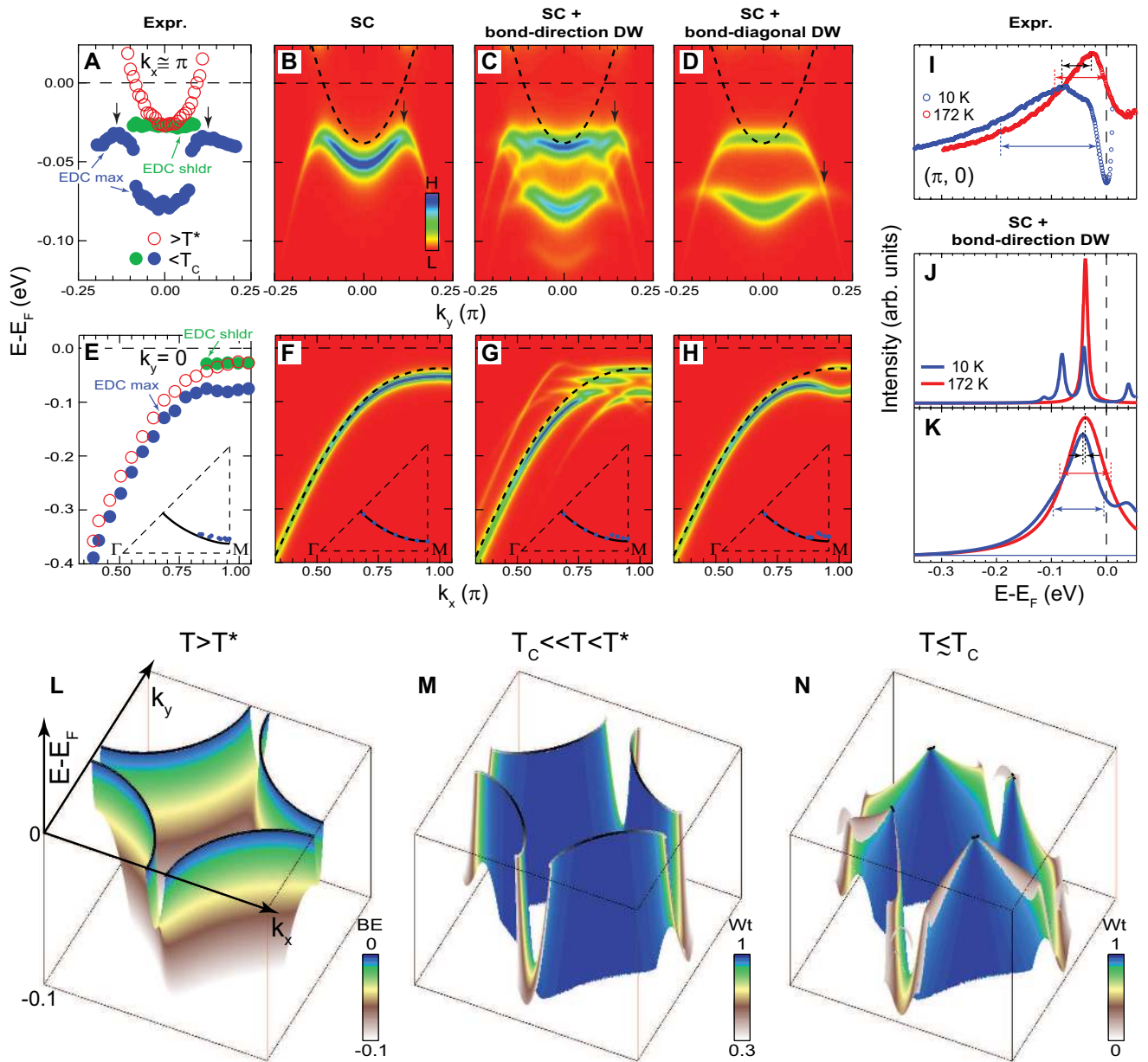
18

Figure S 6: **ARPES simulation on the $k_G - k_F$ misalignment issue.** Even in a Bardeen-Cooper-Schrieffer (BCS) superconductor, **1)** a finite shift in k_F can result from a finite shift in the chemical potential assuming a particle number conservation in the gapped state. We find that the chemical potential increases by 5 meV in the superconducting state ($\Delta = 35$ meV), which results in an effective bare band at low temperature (dashed black curve) with an increased k_F relative to the bare band in the ungapped state (solid black curve). This increase is too small to be able to account for the $k_G - k_F$ misalignment experimentally observed; **2)** a finite $k_G - k_F$ misalignment can in principle result from a finite momentum dependence of the superconducting order parameter along the cut. Again this effect alone is negligible in our case, as shown by the simulated false-color plot for the spectral function: the EDC peak dispersion (red dotted curve) shows a back-bending with k_G very close to k_F (of the solid black curve); **3)** this simulation with realistic experiment conditions (see the **Simulations** part) also rules out a trivial interpretation of the observed $k_G - k_F$ misalignment due to finite energy, momentum resolutions and quasiparticle lifetime.

Figure S 7 *(following page)*: **Simulations for the superconductivity-density-wave coexistence.** **A & E**, Summary of experimental dispersions at 10 K and 172 K along Cut C1 (reproduction of Fig. 2O) and P1-P16 (Fig. 2V-W), respectively. **B & F, C & G, D & H**, Renormalized band dispersions by simulations assuming different long-range orders: d-wave superconductivity (SC, $\Delta = 35$ meV), its coexistence with bond-direction $q_1 = (0.15\pi, 0)$ & $q_2 = (0, 0.15\pi)$ checkerboard density wave (DW, $V_1 = 20$ meV) or with bond-diagonal $q_{AF} = (\pi, \pi)$ density wave ($V_2 = 35$ meV), respectively, perpendicular to or along Γ-M. Dashed curves are bare band dispersions resulting from a global tight-binding fit to the experimental EDC peak dispersions at 172 K (Fig. 5). Renormalized band dispersions are moderately broadened for visualization purpose and the intensity reflects intrinsic spectral weight. Note that the visual separation between dominant states at low and high energies is not a real hybridization gap but due to suppression of intrinsic spectral weight of dispersions within (**C-D**). Insets of **E-H**: k_G (arrows in **A-D**) shown in half of a quadrant, from the experiment and simulations. Apparent discontinuities in the insets of **G-H** are due to changes of the physical character of back-bending. Error bars are smaller than the symbol size. **I-K**, Comparison between experimental and simulated EDCs at M point at 10 K and 172 K. Experimental intensity is normalized by the incident photon flux. Simulated EDCs in **J** are obtained from **G**, which are broadened phenomenologically in **K** (see the **Simulations** part). Different arrows are eyeguides for the EDC linewidth and energy shift of the EDC centroid. In **K**, multiple features below E_F at low temperature merge into a single feature, with its centroid energy and overall linewidth barely changed from high temperature, still very different from the experiment (**I**). **L-N**, Cartoons for the evolving band structure in different phases. Fermi surface is shown in black at E_F. Color scale is proportional to the intrinsic spectral weight in **M & N**. A (π, π) density wave order ($V_2 = 50$ meV) and its coexistence with d-wave superconductivity ($\Delta = 35$) are assumed in **M & N**, respectively, only for illustrative purpose. Note that the values of parameters in all simulations are chosen only for a qualitative agreement with the experiment.

Expr.

A $k_x \cong \pi$

EDC shldr

EDC max

○ >T*
● <T_C

B SC

H

L

C SC +
bond-direction DW

D SC +
bond-diagonal DW

E $k_y = 0$

EDC shldr

EDC max

Γ   M

F

Γ   M

G

Γ   M

H

Γ   M

k_y (π)

k_x (π)

$E-E_F$ (eV)

I Expr.

○ 10 K
○ 172 K

(π, 0)

J SC +
bond-direction DW

10 K
172 K

K

$E-E_F$ (eV)

L T>T*

k_y

$E-E_F$

k_x

BE
0

-0.1

M T_C<<T<T*

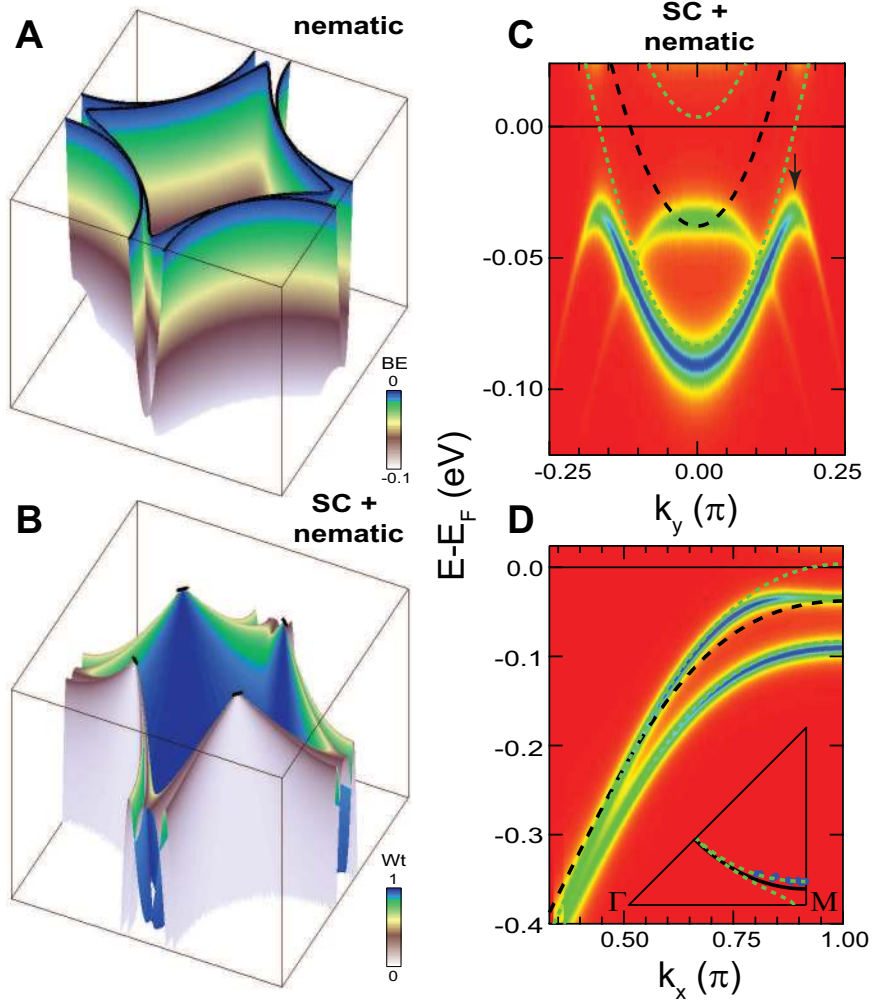Wt
1

0.3

N T≲T_C

Wt
1

0

21

Figure S 8: **Simulations for the superconductivity-nematic-order coexistence.** **A** (**B**), Cartoon for the band structure in the nematic phase without (with) coexisting d-wave superconductivity ($\Delta = 35$ meV). Two sets of bands from orthogonal domains are superimposed. **C** (**D**), Renormalized band dispersions perpendicular to (along) Γ-M in the coexisting state. Black (green) dashed curves are the bare (distorted) band dispersions. Renormalized band dispersions are moderately broadened for visualization purpose. Back-bending is pointed out by arrow. Insets: k_G from the experiment that falls on the distorted Fermi surface in green. Color scale is proportional to the intrinsic spectral weight in **B**-**C**. Note that the values of parameters in the simulation are chosen only for a qualitative agreement with the experiment.

References and Notes

S1. T. Kondo, T. Takeuchi, S. Tsuda, S. Shin, *Phys. Rev. B* **74,** 224511 (2006).

S2. M. Hashimoto *et al.*, *Phys. Rev. B* **77,** 094516 (2008).

S3. M. Hashimoto *et al.*, *Nat. Phys.* **6,** 414 (2010).

S4. J.-H. Ma *et al.*, *Phys. Rev. Lett.* **101,** 207002 (2008).

S5. T. Kondo, R. Khasanov, T. Takeuchi, J. Schmalian, A. Kaminski, *Nature* **457,** 296 (2009).

S6. S. Ono, Y. Ando, *Phys. Rev. B* **67,** 104512 (2003).

S7. G.-q. Zheng, P. L. Kuhns, A. P. Reyes, B. Liang, C. T. Lin, *Phys. Rev. Lett.* **94,** 047006 (2005).

S8. J. Xia, P. T. Beyersdorf, M. M. Fejer, A. Kapitulnik, *Appl. Phys. Lett.* **89,** 062508 (2006).

S9. J. Xia, Y. Maeno, P. T. Beyersdorf, M. M. Fejer, A. Kapitulnik, *Phys. Rev. Lett.* **97,** 167002 (2006).

S10. J. Xia *et al.*, *Phys. Rev. Lett.* **100,** 127002 (2008)

S11. V. Hinkov *et al.*, *Science* **319,** 597 (2008).

S12. J. E. Sonier, *Phys. Rev. B* **66,** 134501 (2002).

S13. N. Gedik *et al.*, *Phys. Rev. B* **70,** 014504 (2004).

S14. J. Voit *et al.*, *Science* **290,** 501 (2000).

S15. H.-D. Chen, O. Vafek, A. Yazdani, S.-C. Zhang, *Phys. Rev. Lett.* **93,** 187002 (2004).

S16. D. F. Agterberg, H. Tsunetsugu, *Nat. Phys.* **4,** 639 (2008).

S17. E. Berg, E. Fradkin, S. A. Kivelson, *Phys. Rev. B* **79,** 064515 (2009).

S18. R. H. He *et al.*, *Phys. Rev. B* **69,** 220502(R) (2004).

S19. A. A. Kordyuk, S. V. Borisenko, M. Knupfer, J. Fink, *Phys. Rev. B* **67,** 064504 (2003).

S20. S. Kawasaki, C. Lin, P. L. Kuhns, A. P. Reyes, G.-q. Zheng, *Phys. Rev. Lett.* **105,** 137002 (2010).

S21. S. Chakravarty, R. B. Laughlin, D. K. Morr, C. Nayak, *Phys. Rev. B* **63,** 094503 (2001).

S22. C. M. Varma, *Phys. Rev. B* **55,** 14554 (1997).

S23. R. Daou *et al.*, *Nature* **463,** 519 (2010).

S24. C. Howald, H. Eisaki, N. Kaneko, A. Kapitulnik, *Proc. Natl. Acad. Sci.* **100,** 9705 (2003).

S25. M. J. Lawler *et al.*, *Nature* **466,** 347 (2010).

S26. B. Fauqu*é et al.*, *Phys. Rev. Lett.* **96,** 197001 (2006).

S27. Y. Li *et al.*, *Nature* **455,** 372 (2008).

S28. J. M. Tranquada, B. J. Sternlieb, J. D. Axe, Y. Nakamura, S. Uchida, *Nature* **375,** 561 (1995).

S29. L. Li *et al.*, *Phys. Rev. B* **81,** 054510 (2010).

S30. J. Corson, R. Mallozzi, J. Orenstein, J. N. Eckstein, I. Bozovic, *Nature* **398,** 221 (1999).

S31. J. Lee *et al.*, *Science* **325,** 1099 (2009).

S32. T. Kondo, T. Takeuchi, A. Kaminski, S. Tsuda, S. Shin, *Phys. Rev. Lett.* **98,** 267004 (2007).